sciendo
Austrian Journal of Earth Sciences | Vienna | 2025 | Volume 118 | 133–139 | DOI: 10.17738/ajes.2025.0007

New single-crystal X-ray diffraction and Raman spectroscopic data of natural bismoclite BiOCl

Irene Liebhart[1], Branko Rieck[1], Manuela Zeug[1,2], and Gerald Giester[1*]

[1)] Department of Mineralogy and Crystallography, University of Vienna, Josef-Holaubek-Platz 2, 1090 Wien, Austria;
[2)] Landesamt für Geologie und Bergwesen, An der Fliederwegskaserne 13, 06130 Halle (Saale), Germany.
[*)] Corresponding author: gerald.giester@univie.ac.at

Keywords: bismoclite, BiOCl, Lavrion mining district, single-crystal X-ray data, Raman spectroscopy

Abstract

The structure of bismoclite BiOCl from the Jean Baptiste mine, Lavrion area, Greece, was characterised by single-crystal X-ray diffraction. The mineral is tetragonal, space group *P4/nmm* with unit-cell parameters a = 3.887 (2), c = 7.357 (5) Å, Z = 2, V = 111.16 (14) Å^3 (R_1 = 0.0134 and wR_2 = 0.0363). Bismoclite is isostructural with the mineral matlockite PbFCl. Chemical analyses showed in some cases partial substitution of Bi by Ca and traces of Fe incorporated. A Raman spectrum of bismoclite reveals the most intense Raman band at 144 cm^{-1} and additional bands of lower intensity at 198 and 396 cm^{-1}.

1. Introduction

Bismuth as an essential component of minerals has been reported thus far for 250 species according to the IMA Mineral List (2025). The majority of them belonging to sulphides and sulfosalts (154), oxides (24), sulphates (16) and the group of phosphates, arsenates and vanadates (37). Bismuth halides (5) are rather rare; examples include gananite BiF_3, zavaritskite BiOF and bismoclite BiOCl.

Synthetic BiOCl as a layer-structured semiconductor is known for various potential technical applications due to its special electrical, magnetic, optical, luminescent and catalytic properties (cf. Tian et al., 2012 and literature cited therein). Studies focus on its suitability as a photocatalytic material (Liu and Peng, 2020; Xu et al., 2022, 2024; Wu et al., 2023; Gordon et al., 2024, Pare et al., 2024; He et al., 2024), light emitting phosphors (Halappa et al., 2019; Wang et al., 2019) or for its dielectric properties (Unuma et al., 2020; Nalawade et al., 2020).

Bismoclite BiOCl was first discovered and described as a new mineral from Jakkalswater, South Africa (Mountain, 1935) on a specimen kept at the McGregor Museum, Kimberley. Bannister and Hey (1935) synthesised BiOCl. The crystal structure was solved on these lab-grown samples by X-ray photographs in space group *P4/nmm* with unit-cell dimensions a = 3.89 and c = 7.37 Å proving isotypy with matlockite PbFCl (Bannister and Hey, 1934). Later, the structure was refined on synthetic material by single-crystal X-ray diffraction with unit-cell data a = 3.887 (5), c = 7.354 (5) Å, R = 9.17% (Keramidas et al., 1993) and by powder X-ray diffraction (PXRD) a = 3.892 (2), c = 7.371 (2) Å, R_p = 3.51% (Halappa et al., 2019). New studies (Testa et al., 2016) on bismoclite from a Bi-Cu-Au deposit, Argentina, included infrared analysis, thermal analysis using DTA and TGA, chemical analysis via inductively coupled plasma mass spectrometry (ICP-MS) and instrumental neutron activation analysis (INAA), as well as scanning electron microscopy (SEM) and PXRD.

The bismoclite group (Dana classification 10.02.01; Gaines et al., 1997) moreover includes the isotypic minerals zavaritskite BiOF (Dolomanova et al., 1962; Aurivillius, 1964; Yatimov et al., 2022), and daubréeite BiO(OH,-

Cl) (Domeyko, 1876; Bannister and Hey, 1935). Besides matlockite PbFCl (Bannister and Hey, 1934; Pasero and Perchiazzi, 1996), bismoclite is further isostructural with the minerals rorisite CaFCl (Liebich and Nicollin, 1977; Kulikov et al., 1982; Chesnokov et al., 1990), zhangpeishanite BaFCl (Sauvage, 1974; Shimazaki et al., 2008) and a large number of synthetic compounds with a triple combination following the matlockite-type system *MFX* (*M* = Ca, Sr, Ba, Sm, Eu, Pb; *X* = Cl, Br, I) (Weil and Kubel, 2001).

In the Lavrion Mining District numerous ore types, such as intrusion-hosted, skarn-, carbonate-replacement, and vein-type ores, can be found (see Voudouris, 2021 and the references therein). This area comprises the western part of the Attic-Cycladic metamorphic core complex, which includes base- and precious-metal skarn, intrusion-related, and epithermal mineralisations. When the metamorphic core complexes were uplifted to near-surface levels over the south-west retreating Hellenic subduction zone, extensional kinematic conditions partially controlled the plutonic and arc-related subvolcanic rocks that are spatially associated with these mineral occurrences (Neubauer, 2005). Recently, bismoclite was reported from the Jean Baptiste mine, Lavrion, Greece (Rieck et al., 2018); this material now for the first time allowed a modern single-crystal X-ray diffraction study on a natural sample.

Figure 1: A map showing the Lavrion Mining District (which corresponds exactly to that of the Lavreotiki UNESCO Global Geopark) as grey shaded area at the tip of the Attika peninsula. The occurrences of bismoclite are marked.

2. Occurrence and material

Bismoclite is proven from various localities worldwide; within Europe, the mineral has been reported from Austria, France, Germany, Italy, Norway, Poland, Spain, UK, and Greece. For Austria, bismoclite has been mentioned from a small, ancient quartz quarry with subordinate copper mineralisation in a quartz layer located southwest of Wolfgruben in the Leoben District, Styria, at an elevation of approximately 770 m above sea level. It is there observed as a secondary product of an unnamed Bi_2Te phase in galena matrix, only a few µm in size (Auer, 2019).

The Lavrion mining district (Fig. 1), Attika, Greece, is known for the presence of bismoclite, also found as a secondary mineral, formed by Cl-bearing aqueous solutions altering primary Bi-bearing minerals, although only in small quantities without any economic significance. At the Kamariza mines in Agios Konstantinos, bismoclite was discovered (Fig. 2) in 2014 on the 2nd level of the Jean Baptiste Mine (Rieck et al., 2018). The primary Bi-bearing mineral was maldonite Au_2Bi. Its breakdown led to the formation of native gold and native bismuth, which in turn was altered to numerous Bi-bearing secondary minerals. Among these, bismoclite and isostructural zavaritskite BiOF are present. Figure 3 shows well crystallized bismoclite on a matrix of quartz, iron oxides/hydroxides, Sb-bearing bismuthinite Bi_2S_3, Ag-bearing gold, native bismuth and various secondary minerals. Figure 4 illustrates long-bladed crystals of bismoclite in a cavity in preisingerite. From the locality in the Hilarion

Figure 2: Locality of bismoclite in the Jean Baptiste mine, April 2014. © Branko Rieck.

Mine, maldonite too is reported as a primary Bi-bearing mineral. However, there is evidence that other Bi-bearing sulfosalts in large part contributed to the availability of bismuth in the oxidizing environment. A completely different type of occurrence in the Lavrion Mining District is observed in the Sclives Mine where native bismuth and bismuthinite accompany Co-bearing phases in narrow veins (Rieck et al., 2022). Bismoclite has there been identified in µm-sized particles only in polished sections. Finally, the Plaka Mine No. 80 has to be mentioned: the late stage As-Sb-Ag-veins occasionally contain small quanti-

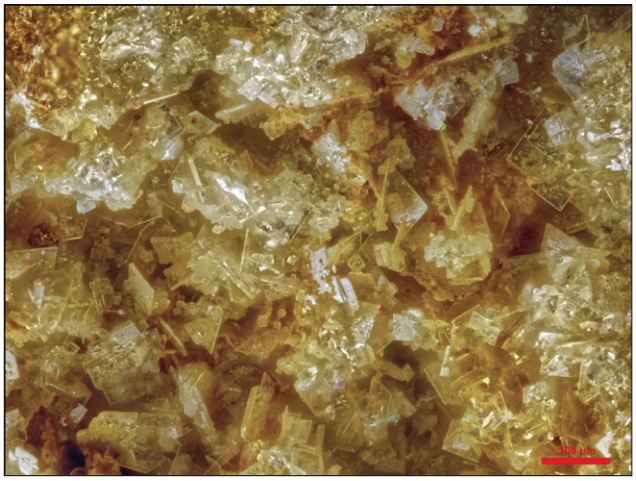

Figure 3: Pale brown, square, thin platy crystals of bismoclite from the Jean Baptiste Mine with small quantities of brown iron oxides/hydroxides (limonite) almost entirely covering the matrix of ore minerals. © Branko Rieck.

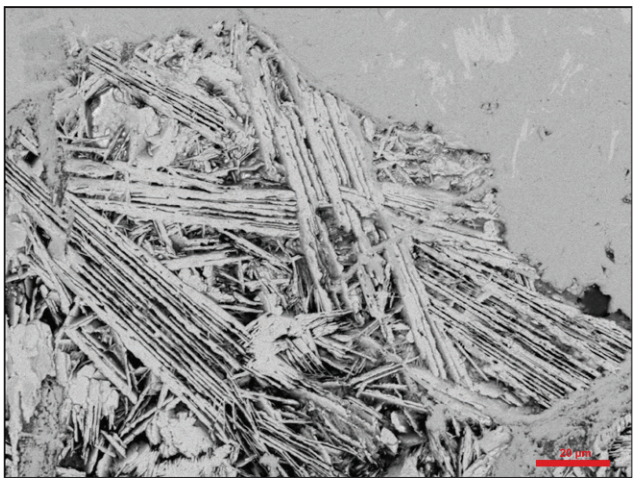

Figure 4: SEM image (scanning electron microscope JEOL JSM-6610LV) of a polished ore section with lamellae of bismoclite in a matrix of preisingerite $Bi_3(AsO_4)_2O(OH)$ which contains small, brighter areas of Cl-bearing bismutite $Bi_2[O_2|CO_3]$ from the 2nd level of the Jean Baptiste Mine. © Uwe Kolitsch.

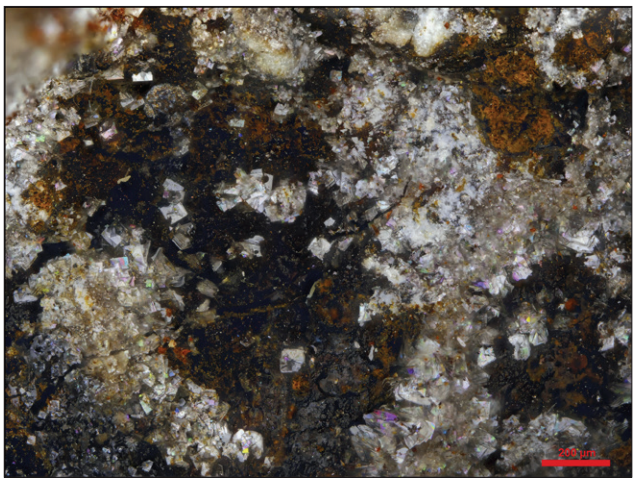

Figure 5: Bismoclite from the Plaka Mine. © Branko Rieck.

ties of native bismuth. While rare, the largest individual grains of native bismuth were found in this environment. Alteration of these veins further produced very well developed crystals of bismoclite (Fig. 5). Especially in the Plaka area, sea-water seeping into the abandoned mines may have contributed to the Cl-content of the fluids responsible for the alteration of the Bi-bearing minerals.

3. Methods

3.1 Raman spectroscopy

Raman spectra (Fig. 6) were collected at room temperature using a dispersive LabRAM HR Evolution spectrometer. The system was equipped with Olympus BX-series microscope, 1800 grooves per millimetre diffraction grating and Peltier-cooled charge-coupled device (CCD) detector. Spectra were excited using a 532-nm emission of a frequency-doubled Nd^{3+}:YAG laser (17 mW at the

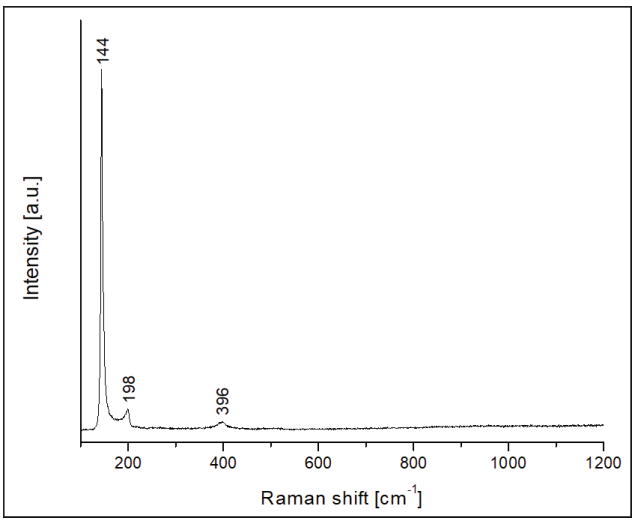

Figure 6: Raman spectrum (532 nm excitation) of bismoclite.

sample surface). A 50× objective (numerical aperture 0.55, free working distance 10.6 mm) was used to obtain Raman spectra. The resulting laser-power density was well below the threshold of absorption-induced sample changes. In view of the large crystal sizes, the system was operated in non-confocal mode. For more details see Zeug et al. (2018).

3.2 Chemical analysis

Bismoclite was studied by WDS (wavelength-dispersive X-ray spectrometry) on an EMPA (electron probe microanalyzer) JEOL Hyperprobe JXA8530F. The results are based on the average of 14 spot-analyses (10 kV and 20 nA) belonging to seven individual crystal fragments. The large beam diameter of 30 µm was chosen to avoid volatilization of Cl. Reference materials used for calibra-

tion were wollastonite $Ca_3(Si_3O_9)$ for Ca ($K\alpha_1$, $K\alpha_2$, $K\beta_1$), bismuth(III) oxide Bi_2O_3 for Bi ($L\alpha_1$, $L\alpha_2$) and halite NaCl for Cl ($K\alpha_1$, $K\alpha_2$, $K\beta_1$).

3.3 X-ray work

A small fragment (0.03×0.05×0.05 mm^3) of bismoclite from the Jean Baptiste mine was investigated by single-crystal X-ray diffraction analysis on a Bruker Apex II system equipped with a CCD area detector and an Incoatec Microfocus Source IμS (30 W, multilayer mirror, Mo-K_α) at ambient conditions. Several sets of phi- and omega-scans with 2° scanwidth were combined at a crystal-detector distance of 35 mm to achieve respective full sphere data up to 90° 2θ. Data handling with integration and absorption correction by evaluation of multi-scans was done with the Bruker Apex4 suite (Bruker, 2021). The structure model was taken according to Keramidas et al. (1993), i.e., the respective atom positions and labelling were chosen using origin choice 2 at center 2/*m*. The least-squares refinement was done with the SHELXL software (Sheldrick, 2015) implemented in the ShelXle GUI tool (Hübschle et al., 2011).

4. Results

4.1 Raman spectroscopy

A representative Raman spectrum of bismoclite is shown in Figure 3. The most intense Raman band lies at 144 cm^{-1}. This band is relatively sharp (full width at half maximum between 5–6 cm^{-1}) and notably asymmetric toward higher energies. Zhang et al. (2012) and Bunda and Bunda (2014) have assigned this band to an overlap of a (dominating) 144–145 cm^{-1} A_{1g} band with a (minor) E_g-type band at 149–150 cm^{-1}. In addition, there are bands of lower intensity at 198 cm^{-1} and 396 cm^{-1} whose assignment remains controversial. For instance, the 198 cm^{-1} band was interpreted as E_g mode by Tian et al. (2012) and Zhang et al. (2012) whereas Bunda and Bunda (2014) assigned it to an A_{1g}-type vibration. The 396 cm^{-1} band has been discussed by Zhang et al. (2012) who assumed it to be a B_{1g}-E_g combination. The bismoclite band at 60cm^{-1} (assumed to be A_{1g} by Zhang et al. 2012, and E_g by Bunda and Bunda 2014) could not be measured with our equipment, because the edge filter of the Raman system for blocking the Rayleigh-scattered laser light only allows the acquisition of spectra well above 60 cm^{-1} Raman shift. Our spectra do not show significant variations depending on random sample orientation.

4.2 Chemical analysis

The chemical composition of seven bismoclite samples from the Jean Baptiste mine was examined. Within the individual grains, no zonal differences were observed between the core and the rim areas. However, it turned out that the composition of the respective crystals varied noticeably among each other. Two crystal fragments proved to be very low in calcium with a Bi:Ca ratio close to $Bi_{0.98}$:$Ca_{0.02}$. Four samples had significant calcium contents with a molar Bi:Ca ratio of ~0.88:0.12, and in one crystal minor iron contents (~0.02 atoms per formula unit) could be observed as well. None of the samples showed F contents above the detection limit which under the conditions used is 80 ppm (3σ). In all cases, the balance of charges may occur by partial substitution of O^{2-} by Cl^{1-} and/or through the incorporation of hydroxyl anions, although the presence of OH groups could not be verified reliably by IR spectroscopy. Relying on the determination of the Cl content, the average composition of the samples with low Ca is $[Bi_{0.98}Ca_{0.02}][O_{0.98}Cl_{0.02}][Cl_{0.95}(OH)_{0.05}]$.

4.3 Structure refinement

The single-crystal X-ray diffraction analysis of bismoclite confirmed the structure model with the formula BiOCl in space group *P4/nmm* with unit-cell parameters *a* = 3.887 (2), *c* = 7.357 (5) Å, *Z* = 2, *V* = 111.16 (14) $Å^3$. The refinement converged at final values R1 = 0.0134 and wR2 = 0.0363 from 309 unique data with Fo > 4σ(Fo). Based on the structure refinement, the sample examined turned out to be almost Ca-free, with a substitution of Bi by Ca of only 1% which was not considered as significant.

The crystallographic data as well as details of the measurement and refinement are listed in Table 1, the atomic

Crystal Data	**BiOCl**
space group	*P4/nmm*
a (Å)	3.887 (2)
c (Å)	7.357 (5)
V ($Å^3$)	111.16 (14)
Z	2
ρ_{calc} (g cm^{-3})	7.781
μ (MoKα) (mm^{-1})	80.084
Data collection and refinement	
$2\theta_{max}$ (°)	90.7
total measured reflections	10494
R_{int}	0.047
h, k	-7 to 7
l	-14 to 14
unique data	319
data with $F_o>4\sigma(F_o)$	309
variables	10
*R*1 [for $F_o>4\sigma(F_o)$] [1]	0.0134
*wR*2 [for all F_o^2] [1]	0.0363
a, b [1]	0.022, 0.067
$\Delta\rho_{min\ /\ max}$ (e$Å^{-3}$)	-2.56 / 2.94
[1] $R1 = \Sigma \lvert\lvert F_o \rvert - \lvert F_c \rvert\rvert / \Sigma \lvert F_o \rvert$; $wR2 = [\Sigma w(F_o^2 - F_c^2)^2 / \Sigma w(F_o^2)^2]^{½}$; $w = 1 / [\sigma^2(F_o^2) + (a\times P)^2 + b\times P]$; $P = \{[\max(0 \text{ or } F_o^2)] + 2F_c^2\} / 3$	

Table 1: Crystal data and details of the intensity measurement and structure refinement for bismoclite

coordinates and displacement parameters are compiled in Table 2. Selected interatomic distances as well as bond valence calculations (Brese and O'Keeffe, 1991) are given in Tab. 3. Further details of the crystal structure investigation can be obtained from the joint CCDC/FIZ Karlsruhe online deposition service: https://www.ccdc.cam.ac.uk/structures/ by quoting the deposition number 2424842.

Site	x	y	z	U^{eq}	$U^{11} = U^{22}$	U^{33}
Bi	0.25	0.25	0.17044 (2)	0.00824 (6)	0.00801 (7)	0.00868 (8)
O	0.25	0.75	0	0.0079 (5)	0.0072 (7)	0.0093 (11)
Cl	0.25	0.25	0.6500 (2)	0.0125 (2)	0.0132 (3)	0.0111 (4)

Table 2: Atom coordinates and displacement parameters with e.s.d.'s in parentheses for bismoclite. All atoms are located on special Wyckoff positions, i.e. Bi, Cl at 2*c*: and O at 2*b* with site symmetries of 4*mm* and 4*m*2, respectively, therefore U^{12}, U^{13} and U^{23} are zero.

Mineral	(1)	(2)	(3)	(4)	(5)	(6)	(7)
A–*X* (Å) 4×	2.3129 (1)	2.320(4)	2.273 (2)	2.32	2.539 (1)	2.362	2.649
A–*Y* (Å) 4×	3.0495 (6)	3.068 (4)	2.748 (2)	3.028	3.089 (4)	2.963	3.2856
A–*Y**(Å) 1×	3.5283 (15)	3.489 (8)	2.920	3.4854	3.217	3.049	3.1960
v $A^{[8]}$–*XY* (v.u.)	3.07	2.99	2.98	2.79	1.89	1.78	1.95
v $A^{[9]}$–*XYY** (v.u.)	3.13	3.053	3.06	2.83	2.01	1.94	2.21

Table 3: Compilation of bond distances (Å) and bond valence sums v (v.u.) for bismoclite and isostructural minerals. Atoms are listed in the *AXY* system with *A* = Bi^{3+}, Pb^{2+}, Ca^{2+}, Ba^{2+}; *X* = O^{2-}, F^-; *Y* = Cl^-, F^-, OH^-.
(1) Bismoclite BiOCl this study; **(2)** Bismoclite BiOCl Halappa et al., 2019; **(3)** Zavaritskite BiOF Aurivillius et al., 1964; **(4)** Daubréeite BiO(OH,Cl) Bannister, 1935; **(5)** Matlockite PbFCl Pasero and Perchiazzi, 1996; **(6)** Rorisite CaFCl Liebich and Nicollin, 1977; **(7)** Zhangpeishanite BaFCl Sauvage, 1974. ***Y**** Next nearest neighbour capping the tetragonal antiprism.

gles O-Bi-O (4×), Cl-Bi-Cl (4×) and O-Bi-Cl (8×) are 72.91, 79.18 and 72.50°, respectively. The oxygen atom is tetrahedrally coordinated to 4 Bi^{3+} ions with Bi-O-Bi angles of 107.09 and 114.34°, (each 3×).

The BiO_4Cl_4 polyhedra share faces and edges to form double-layers parallel (001) as illustrated in Figure 7. Bond valences to oxygen and chlorine sum up to 2.21 and 0.86

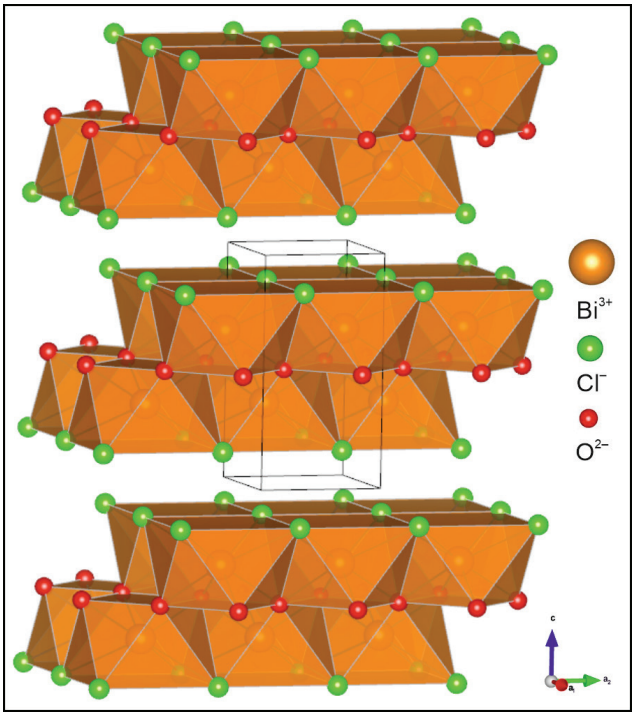

Figure 7: Crystal structure of bismoclite, illustrating the arrangement of the BiO_4Cl_4 antiprisms, sharing faces and edges to form double-layers parallel (001).

5. Discussion

The Raman spectrum of bismoclite from Lavrion corresponds well with the spectrum of bismoclite from Antofagasta, Chile, in the RRUFF database (www.rruff.info, accessed on 11 December 2024; spectrum R100197). Additionally, it corresponds to spectra of synthetic BiOCl obtained by Bunda and Bunda (2014), and the identically composed "bismuth white" pigment (Burgio, 2024). Band positions and relative intensities observed herein (most intense band at 144 cm^{-1}, and weaker ones at 198 cm^{-1} and 396 cm^{-1}) concur well with Raman parameters of "bismuth white" observed by Burgio (2024; intense at 145 cm^{-1}, and weak at 199 cm^{-1} and 398 cm^{-1}). Although the Raman fingerprint pattern consists of only a few bands, it is very characteristic and enables fast and reliable mineral identification.

In the structure of bismoclite all atoms are located on special positions: the Wyckoff sites are 2*c* for Bi, Cl and 2*b* for O with site symmetries of 4*mm* and 4*m*2, respectively. The atomic arrangement is characterised by Bi^{3+} cations, coordinated to each four O^{2-} and Cl^- ligands – located on opposite sides – to form a tetragonal antiprism. Bond angles O-Bi-O (4×), Cl-Bi-Cl (4×) and O-Bi-Cl (8×) are 72.91, 79.18 and 72.50°, respectively. The oxygen atom is tetrahedrally coordinated to 4 Bi^{3+} ions with Bi-O-Bi angles of 107.09 and 114.34°, (each 3×).

The BiO_4Cl_4 polyhedra share faces and edges to form double-layers parallel (001) as illustrated in Figure 7. Bond valences to oxygen and chlorine sum up to 2.21 and 0.86 v.u., respectively. This asymmetric coordination is influenced by the $6s^2$ lone electron pair of Bi^{3+}, not involved in chemical bonding. Cations with ns^2 electron pair (Tl^{1+}, Pb^{2+}, Sn^{2+}, As^{3+}, Bi^{3+}, Sb^{3+}, Se^{4+}, Te^{4+}, Br^{5+}, I^{5+}), respectively, are commonly asymmetrically coordinated due to stereochemical activities of electrons. (Orgel, 1959; Galy et al., 1975). This effect is also observable for related minerals of bismoclite (see Tab. 3).

The coordination polyhedron of the isostructural mineral matlockite PbFCl is commonly described as monocapped square antiprism (Pasero and Perchiazzi, 1996). This takes into account that the bond valence contribution of the 9th ligand (Cl) is distinct. Even more pronounced as in matlockite, this is evident for the minerals rorisite CaFCl and zhangpeishanite BaFCl. Within the isotypic matlockite series the bond valence saturation of the cation significantly increases through the contribution of the 9th ligand; respective sums of bond valences for matlockite, rorisite and zhangpeishanite are listed in Table 3. These interactions are particularly responsible for linking the double-layers. For the bismoclite group the descrip-

tion of bismuth with eight ligands, forming a tetragonal antiprism, seems appropriate. The bond valence sums for Bi in bismoclite, zavaritskite and daubréeite are 3.07, 2.98 and 2.79 v.u., respectively. However, the bond valence contributions of an additional 9th ligand are only 0.059, 0.081, and 0.045 v.u. for bismoclite, zavaritskite and daubréeite, respectively, and considered as moderate to rather weak, although have to be taken into account for structural cohesion.

6. Conclusions

The occurrence of the rare mineral species bismoclite BiOCl from the Jean Baptiste mine in Agios Konstantinos, Attica, also highlights the uniqueness of the Lavrion mining district. The single-crystal X-ray diffraction analysis confirms the crystal structure of the bismuth oxyhalide phase on a natural sample and the Raman spectrum can be useful to identify bismoclite.

Acknowledgements

We thank Lutz Nasdala for helpful discussions improving the manuscript and Eugen Libowitzky for IR measurements. The SEM image of bismoclite from the Jean Baptiste Mine was kindly provided by Uwe Kolitsch.

References

Auer C., 2019. Die Mineralien der Wolfsgrube bei Seiz im Liesingtal. Der Steirische Mineralog 34, 5–11.

Aurivillius B., 1964. The Crystal Structure of Bismuth Oxide Fluoride II. A Refinement of the Previously Published Structure. Acta Chemica Scandinavica, 18/8, 1823–1830. DOI:10.3891/acta.chem.scand.18-1823

Bannister F.A., Hey M.H., 1934. The crystal-structure and optical properties of matlockite (PbFCl). Mineralogical Magazine and Journal of the Mineralogical Society 23/146, 587–597. https://doi.org/10.1180/minmag.1934.023.146.02

Bannister F.A., Hey M.H., 1935. The crystal-structure of the bismuth oxyhalides. Mineralogical Magazine and Journal of the Mineralogical Society 24/149, 49–58. https://doi.org/10.1180/minmag.1935.024.149.01

Brese N.E, O'Keeffe M., 1991. Bond-Valence Parameters for Solids. Acta Crystallographica B47, 192–197. https://doi.org/10.1107/S0108768190011041

Bruker 2021. APEX4. Bruker AXS Inc., Madison, Wisconsin, USA.

Bunda S., Bunda V., 2014. Raman Spectra of Bismuth Oxyhalide Single Crystals. Acta Physica Polonica A126, 272–273. https://doi.org/10.12693/APhysPolA.126.272

Burgio L., 2024. Bismuth white (bismuth oxychloride) and its use in portrait miniatures painted by George Engleheart. Minerals 14, 723. https://doi.org/10.3390/min14070723

Chesnokov B.V., Nishanbaev T.P., Bazhenova L.F., 1990. Rorisite CaFCl – novyj mineral. Zapiski Vsesoûznogo Mineralogičeskogo Obŝestva 119/3, 73–76.

Dolomanova E.I., Senderova V.M., Yanchenko M.T., 1962. Zavaritskite (BiOF), a new mineral from the group of oxyfluorides. Dokl. Akad. Nauk Ukr. SSR, 1962, 146/3, 680–682.

Domeyko I., 1876. Daubréeite (oxychlorure de bismuth) – espèce minérale nouvelle. Comptes Rendus Hebdomadaires des Séances de l'Académie des Sciences 82, 922–923.

Gaines R.V., Skinner H.C.W., Foord E.E., Mason B., Rosenzweig A., 1997. Dana's New Mineralogy: The System of Mineralogy of James Dwight Dana and Edward Salisbury Dana. Wiley-Interscience, New. 8th Revised ed., 1819pp.

Galy J., Meunier G., Andersson S., Åström A., 1975. Stéréochimie des eléments comportant des paires non liées: Ge (II), As (III), Se (IV), Br (V), Sn (II), Sb (III), Te (IV), I (V), Xe (VI), Tl (I), Pb (II), et Bi (III) (oxydes, fluorures et oxyfluorures). Journal of Solid State Chemistry 13/1–2, 142–159. https://doi.org/10.1016/0022-4596(75)90092-4

Gordon M.N., Junkers L.S., Googasian J.S., Mathiesen J.K., Zhan X., Morgan D.G., Jensen K.M.Ø., Skrabalak. S.E., 2024. Insights into the nucleation and growth of BiOCl nanoparticles by *in situ* X-ray pair distribution function analysis and *in situ* liquid cell TEM. Nanoscale 16, 15544–15557. https://doi.org/10.1039/D4NR01749H

Halappa P., Rajashekar H.M., Shivakumara C., 2019. Synthesis and structural characterization of orange red light emitting Sm^{3+} activated BiOCl phosphor for WLEDs applications. Journal of Alloys and Compounds, 785, 169–177. https://doi.org/10.1016/j.jallcom.2019.01.155

He Y., Men D., Pang Y., Guo H., Gu J., Li A., 2024. Sample Fabrication of BiOCl Nanosheets with Low Specific Surface Area for Efficient Photocatalytic Degradation of Organic Wastewater. Langmuir 40/32, 16900–16908. https://doi.org/10.1021/acs.langmuir.4c01507

Hübschle C.B., Sheldrick G.M., Dittrich B., 2011. ShelXle: a Qt graphical user interface for SHELXL. Journal of Applied Crystallography 44, 1281–1284. https://doi.org/10.1107/S0021889811043202

IMA Mineral List, 2025. IMA Database of Mineral Properties. Created and maintained by the RRUFF Project in partnership with the IMA. (https://rruff.info/ima/) as of 2025.03.13.

Keramidas K.G., Voutsas G.P., Rentzeperis P.I., 1993. The crystal structure of BiOCl. Zeitschrift für Kristallographie 205, 35–40. https://doi:10.1524/zkri.1993.205.part-1.35

Kulikov I.V., Devyatov V.E., Gromov A.V., 1982. A new natural compound calcium-fluoride-chloride. Izvestiya Vysshikh Uchebnykh Zavedenii. Geologiya i Razvedka 25, 120–122.

Liebich B.W., Nicollin D., 1977. Refinement of the PbFCl types BaFI, BaFBr and CaFCl. Acta Crystallographica B33/9, 2790–2794. https://doi.org/10.1107/S0567740877009480

Liu W-W., Peng R-F., 2020. Recent advances of bismuth oxychloride photocatalytic material: Property, preparation and performance enhancement. Journal of Electronic Science and Technology 18, 100020. https://doi.org/10.1016/j.jnlest.2020.100020

Mountain E. D., 1935. Two new bismuth minerals from South Africa. Mineralogical magazine and journal of the Mineralogical Society 24/149, 59–64. https://doi.org/10.1180/minmag.1935.024.149.02

Nalawade Y., Pepper J., Harvey A., Griffin A., Caffrey D., Kelly A.G., Coleman J.N., 2020. All-Printed Dielectric Capacitors from High-Permittivity, Liquid-Exfoliated BiOCl Nanosheets. Applied Electronic Materials 2/10, 3233–3241. https://doi.org/10.1021/acsaelm.0c00561

Neubauer F., 2005. Structural control of mineralization in metamorphic core complexes. In: Mao J., Bierlein F.P. (editors) Mineral deposit research: meeting the global challenge. Springer, Berlin, 561–564. https://doi.org/10.1007/3-540-27946-6_144

Orgel L.E., 1959. 769. The stereochemistry of B subgroup metals. Part II. The inert pair. Journal of the Chemical Society (Resumed), 3815–3819. https://doi.org/10.1039/JR9590003815

Pare B., Joshi R., Mehta S., Solanki V.S., Gupta R., Agarwal N., Yadav V.K., 2024. Preparation and characterisation of BiOCl nano photocatalyst for the remediation of wastewater under LED light. International Journal of Environmental Analytical Chemistry. https://doi.org/10.1080/03067319.2024.2442086

Pasero M., Perchiazzi N., 1996. Crystal structure refinement of matlockite. Mineralogical Magazine 60, 833–836. https://doi.org/10.1180/minmag.1996.060.402.15

Rieck B., Kolitsch U., Voudouris P., Giester G., Tzeferis P., 2018. Weitere Neufunde aus Lavrion, Griechenland. Mineralien Welt, 29/5, 32–77.

Rieck B., Kolitsch U., Voudouris P., Giester G., Tzeferis P., 2022. Neubestimmung aus dem Bergbaubezirk Lavrion, Griechenland. Mineralien Welt 33/5, 6–20.

Sauvage M., 1974. Refinement of the structures of SrFCl and BaFCl. Acta Crystallographica B30/11, 2786–2787. https://doi.org/10.1107/S0567740874008132

Sheldrick G.M., 2015. Crystal structure refinement with SHELXL.

Acta Crystallographica C71, 3–8. https://doi.org/10.1107/S2053229614024218

Shimazaki H., Miyawaki R., Yokoyama K., Matsubara S., Yang Z., 2008. Zhangpeishanite, BaFCl, a new mineral in fluorite from Bayan Obo, Inner Mongolia, China. European Journal of Mineralogy 20/6, 1141–1144. https://doi.org/10.1127/0935-1221/2009/0021-1888

Testa F.J., Cooke D.R., Zhang L-J., Mas G.R., 2016. Bismoclite (BiOCl) in the San Francisco de los Andes Bi-Cu-Au Deposit, Argentina. First Occurrence of a Bismuth Oxychloride in a Magmatic-Hydrothermal Breccia Pipe and Its Usefulness as an Indicator Phase in Mineral Exploration. Minerals 6/3, 62. https://doi.org/10.3390/min6030062

Tian Y., Guo C.F., Guo Y., Wang Q., Liu Q., 2012. BiOCl nanowire with hierarchical structure and its Raman features. Applied Surface Science, 258, 1949–1954. https://doi.org/10.1016/j.apsusc.2011.06.137

Unuma T., Sasaki T., Yamaki K., Irie A., Ishida H., Kato T., 2020. Dielectric properties of crystalline BiOCl in the terahertz region. OSA Continuum 3/9, 2646–2652. https://doi.org/10.1364/OSAC.399616

Voudouris P., Melfos V., Mavrogonatos C., Photiades A., Moraiti E., Rieck B., Kolitsch U., Tarantola A., Scheffer C., Morin D., et al. 2021. The Lavrion Mines: A Unique Site of Geological and Mineralogical Heritage. *Minerals, 11/1,* 76, 1–22. https://doi.org/10.3390/min11010076

Wang Q., Xie M., Min X., Huang Z., Liu Y., Wu X., Fang M., 2019. Synthesis, structural, and luminescence properties of BiOCl:Dy^{3+} single-component white-light-emitting phosphor for n-UV w-LEDs. Chemical Physics Letters 727, 72–77. https://doi.org/10.1016/j.cplett.2019.04.047

Weil M., Kubel F., 2001. Matlockite-type PbFI. Acta Crystallographica E57/9, i80-i81. https://doi.org/10.1107/S1600536801013678

Wu Q., Luo L., Li W., Peng Du P., 2023. Construction of Er^{3+}-activated BiOCl upconverting microplates with boosted visible-near-infrared light driven photocatalytic activity for tetracycline degradation. Journal of Alloys and Compounds, 932, 167617. https://doi.org/10.1016/j.jallcom.2022.167617

Xu Z., Zhang C., Zhang Y., Gu Y., An Y., 2022. BiOCl-based photocatalysts: Synthesis methods, structure, property, application, and perspective. Inorganic Chemistry Communications, 138, 109277. https://doi.org/10.1016/j.inoche.2022.109277

Xu L., Yu J.C., Wang Y., 2024. Recent advances on bismuth oxyhalides for photocatalytic CO_2 reduction. Journal of Environmental Sciences 140, 183–203. https://doi.org/10.1016/j.jes.2023.07.002

Yatimov U.A., Belogub E.V., Shilovskikh V.V., Blinov I.A., 2022. Zavaritskite from Sulfide-Magnetite Ore of the Aktash Skarn Deposit, Western Karamazar. Geology of Ore Deposits 64/7, 513–518. https://doi.org/10.1134/S107570152207011X

Zeug M., Nasdala L., Wanthanachaisaeng B., Balmer W.A., Corfu F., Wildner M., 2018. Blue zircon from Ratanakiri, Cambodia. Journal of Gemmology, 36/2, 112–132. http://dx.doi.org/10.15506/JoG.2018.36.2.112

Zhang K., Liang J., Wang S., Liu J., Ren K., Zheng X., Luo H., Peng Y., Zou X., Bo X., Li J., Yu X., 2012. BiOCl Sub-Microcrystals Induced by Citric Acid and Their High Photocatalytic Activities. Crystal Growth Design, 12, 793–803. https://doi.org/10.1021/cg201112j

Received: 19.2.2025
Accepted: 29.4.2025
Editorial Handling: Andre Baldermann